Proceedings of ASME:
ASME Turbo Expo 2004 Power for Land, Sea and Air
June 14-17, 2004- Vienna, Austria

GT2004-53086

STATOR DIFFUSION ENHANCEMENT USING A RE-CIRCULATING CO-FLOWING STEADY JET

David Car
AFRL/PRTF
1950 Fifth St. Bldg. 18D
Wright-Patterson AFB, OH 45433

Nicholas J. Kuprowicz
AFRL/PRTA
1950 Fifth St. Bldg. 18D
Wright-Patterson AFB, OH 45433

Jordi Estevadeordal
Innovative Scientific Solutions, Inc.
2766 Indian Ripple Rd.
Beavercreek, OH 45440

Gecheng Zha
University of Miami
Dept. of Mechanical Engineering
Coral Gables, FL 33124

William Copenhaver
AFRL/PRT
1950 Fifth St. Bldg. 18D
Wright-Patterson AFB, OH 45433

ABSTRACT

This paper will outline a steady flow control technique that augments the diffusion process within a stator passage via a continuous co-flowing secondary flow stream along the suction surface. The technique is similar to that used for flow vectoring in nozzles where a secondary flow stream is used to enhance the diffusion and vectoring of high speed jets. Diffusion factors in excess of 0.95 are simulated and the "penalty" for the secondary system is addressed with an availability and simple power analysis. Losses within the secondary flow stream were included in the availability analysis, but it did not account for losses within a delivery system of this secondary flow. This was accomplished through the 1D power analysis which assessed this technique's impact on the efficiency of an axial compression stage and the sensitivity of this efficiency to the secondary flow system's efficiency. Also, a system level analysis is presented to assess the merits that may be realized in a notional engine with this type of flow control. Particularly, impacts on specific fuel consumption and thrust-to-weight ratio were addressed. A cascade experiment was performed to demonstrate the concept and was conducted in a blow-down cascade tunnel. Significant improvements in diffusion were qualitatively seen from the DPIV measurements despite limitations in achieving the desired secondary flow conditions.

INTRODUCTION

The trend to higher stage loading in axial turbomachines continues to put an increasing demand on the stator to provide higher amounts of diffusion. Many researchers are addressing this issue through the use of varying flow control techniques [1-4]. Many of these techniques involve the use of blowing jets or suction devices or a combination of the two to control the amount of separation and thereby increase the diffusion and overall performance of the blade section. There are others who are showing promise using unsteady techniques with synthetic jets to control boundary layer parameters [5,6]. These techniques are very appealing in that they impart a zero net mass change to the core flow. Still others are using plasmas for boundary layer control [7].

The flow control technique outlined in this paper imparts no net mass flow change to the core flow through the use of a re-circulating co-flowing jet that enhances the diffusion and turning levels through its interaction with the core flow. This technique is similar to those used in jet nozzle flow vectoring which create a secondary flow using a suction collar and pump [8-11]. The technique outlined here spawned from the work performed in fluidic vectoring in nozzles and is an attempt to create a similar condition in the stator passage with a re-circulating co-flowing system. It is envisioned that this secondary flow is sustained with a re-circulating secondary flow system as shown in Figure 2.

The "penalty" of this type of arrangement on the overall compression system may not be too great if the required total pressure ratio of the secondary flow system and its efficiency requirement is reasonable. A power and availability analysis was conducted in an attempt to address this issue. Also, a system level analysis using a notional engine configuration is carried out to assess the impact on engine performance. The concern over heating effects caused by the re-circulating flow and the possible need for intercooling the secondary flow was raised in private communications [12]. This technique relies on momentum and heat exchange between the core flow and the secondary flow as it traverses the blade so it may not be

necessary for an intercooler, particularly if the secondary flow system does not require a substantial power input.

A cascade experiment was conducted to evaluate the concept. Shortfalls within the secondary flow system limited the amount of secondary flow, falling short of the desired conditions of the CFD simulations, but a qualitative improvement in diffusion was apparent from DPIV measurements.

.

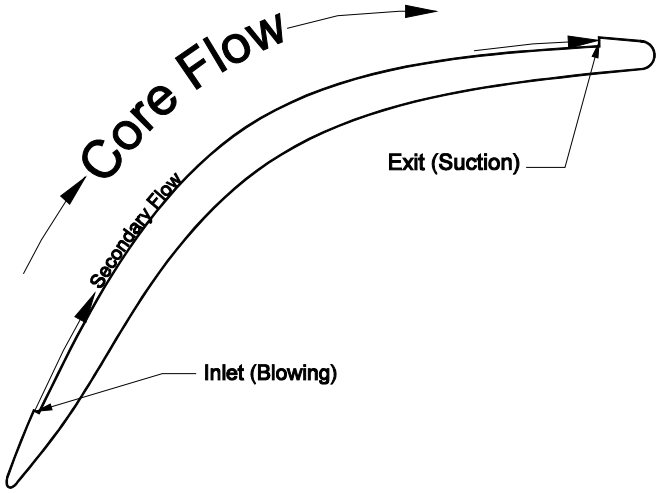

Figure 1 Flow Control Concept

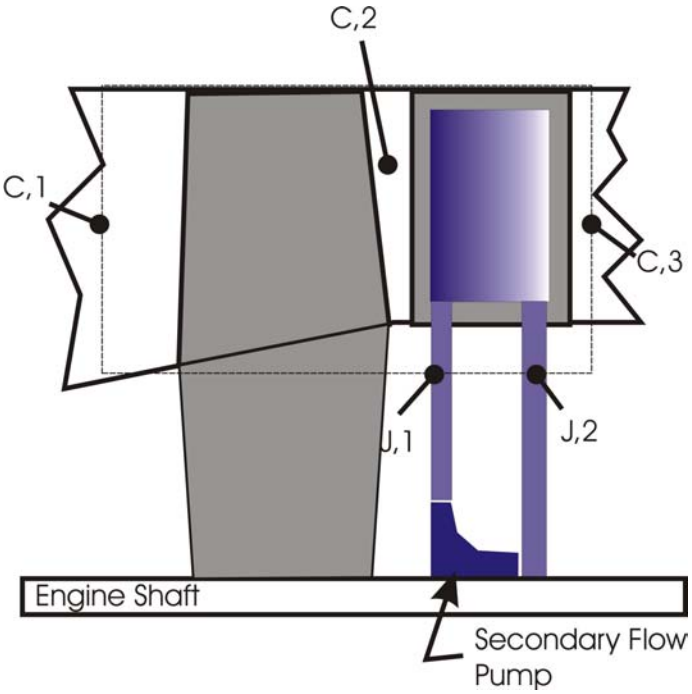

Figure 2 Flow Control Implementation

CONTROL VOLUME ANALYSIS

A 2D control volume analysis was performed to determine the relevant non-dimensional parameters and the influence this flow control technique may have on the core flow. The control volume used is shown in Figure 3. The simplifying assumption is made that the region containing the secondary flow jet is a circular arc and that the inlet and exit velocity of the secondary flow jet is equal. The resulting non-dimensional axial and tangential blade loading equations that result are as follows:

$$F_x^* = 1 - \frac{V_{x2}}{V_{x1}} - c_\mu\left(\sin(\theta_2) - \sin(\theta_1)\right) - C_p$$
$$F_y^* = \Gamma^* + c_\mu\left(\cos(\theta_2) - \cos(\theta_1)\right) \quad (1)$$

where

$$c_\mu = \frac{\rho_j V_j^2 h}{\rho_1 V_{x1}^2 S} = \frac{\dot{m}_j V_j}{\dot{m}_c V_{x1}}$$
$$\Gamma^* = \frac{\left(V_{y1} - V_{y2}\right)S}{V_{x1}S} = \frac{\Gamma}{V_{x1}S}$$
$$F_x^* = \frac{F_x}{\rho_1 V_{x1}^2 S} \qquad F_y^* = \frac{F_y}{\rho_1 V_{x1}^2 S}$$
$$C_p = \frac{P_2 - P_1}{\rho_1 V_{x1}^2}$$

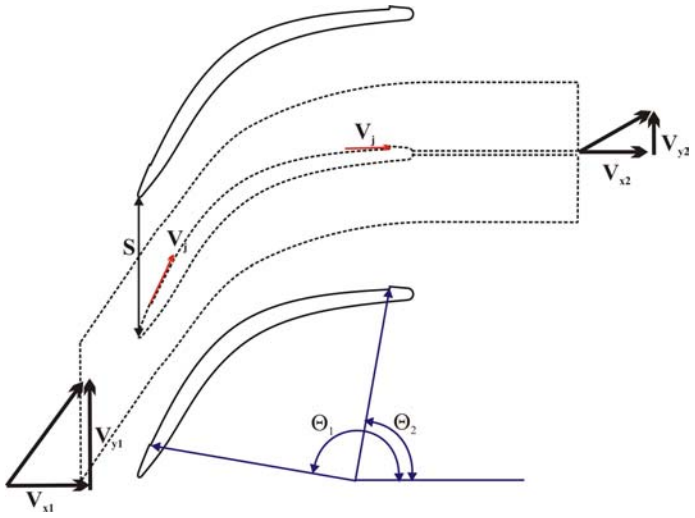

Figure 3 Control Volume

Albeit, the reader will recognize these parameters as the static pressure rise coefficient, C_p; the circulation, Γ^*; the momentum coefficient; c_μ; and the non-dimensional tangential and axial blade loading, F_y^* and F_x^* respectively.

The amount of turning a stator cross section achieves is proportional to the tangential blade loading. The momentum coefficient, c_μ, offers a positive contribution to the tangential blade loading, F_y^*, if and only if it effects Γ^* in a positive

manner, i.e. $\frac{\partial \Gamma}{\partial c_\mu} > 0$. Interestingly, if the secondary flow jet direction were reversed in the control volume analysis, i.e. a counter-flow direction, then the equations remain the same. Also, F_y^* is increased if the angular extent over which the secondary flow region acts is increased.

The momentum coefficient, c_μ, offers a scaleable non-dimensional parameter for the secondary flow system. It's seen in much literature concerning flow control devices; particularly ones involving circulation control airfoils [13,14]. The secondary mass flow must scale with the core mass flow along with the jet velocity to axial velocity ratio in order to hold the momentum coefficient constant. The secondary mass flow could also scale with the engine shaft speed since the core mass flow in an axial compression system is tied to the engine shaft speed and it's envisioned that the secondary flow pump would be tied to the same shaft as shown in Figure 2. Therefore it seems reasonable that the type of configuration shown in Figure 2 could hold c_μ relative constant over the engine operating range. A computational fluid dynamics investigation was performed as a first step in understanding the influence this flow control technique might have on the core flow.

CFD SIMULATIONS

The geometry shown in Figure 3 was simulated using FLUENT, a commercial CFD package. The geometry was created from a series of three circular arcs ensuring continuity of slope between them. The first circular arc extends from 0-10% axial chord; the second from 10-90%; and the third from 90-100%. The overall chord is 0.127 m with a solidity of 1.67. The radius of curvature for each section is as follows: 0.1836 m, 0.0696 m and 0.1841 m. The thickness distribution for the controlled blade was set to allow enough cross sectional area to pass the required secondary flow for a future cascade experiment which would allow full span control. This experiment will be discussed later in this paper.

The simulation was a 2D simulation with a hybrid grid consisting of triangular elements in the core flow with a quadrilateral element O-grid around the blade. The grid system is shown in Fig. 4. The solver setup used k-epsilon turbulence modeling and wall functions to model the boundary layer. For the flow controlled blade, the inset cavity grid was 21x101 and there were a total of 17050 cells in the entire grid domain.

The inlet conditions for this cascade section were a Mach number of 0.7 with an inlet angle of 68 degrees. An axial exiting flow with an approximate Mach number of 0.2 was the desired exit condition. This case would result in an extreme DF of approximately 0.98. The inlet Mach number of 0.7 was chosen because of a future cascade test in which the cascade tunnel was limited to a maximum running Mach number of 0.8.

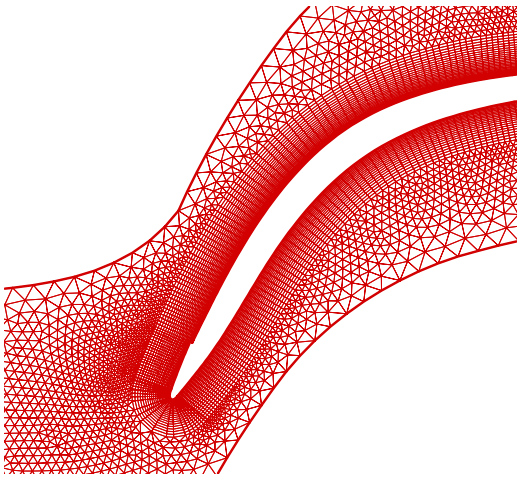

Figure 4 Hybrid CFD Grid

The inlet and exit of the core flow domain and the inset cavity were simulated in the same manner. Both specified the total temperature, pressure and flow angle at the inlet and the static pressure at the exit boundary. The exit static pressures to the core flow and the cavity flow were iterated until the desired inlet Mach number to the core flow was achieved and the exit mass flow to the inset cavity was equal to the inlet mass flow to the cavity. The inlet and exit to the inset cavity are decoupled in this way which is different from the envisioned application requiring a re-circulating pumping system. Time constraints forced us to use the existing boundary conditions provided in the CFD package rather than write custom routines to represent the pumping system and provide feedback to the inlet of the inset cavity. Therefore, the total temperature for the cavity inlet was set to the core flow total temperature thereby not addressing the possible re-heating effects mentioned earlier.

First, a baseline was run to compare against and establish the effectiveness of the flow control technique. The baseline blade was similar in shape to the flow control blade in terms of blade curvature. The suction surface of the baseline blade did not contain the inset cavity and the pressure surface was altered on the flow control blade to provide the necessary cross sectional area for internal cavities for the suction and blowing volume in a future cascade experiment.

The comparison between the flow controlled blade and the baseline blade shape is still valid even though the blade shapes are not exactly the same because: 1) If I were to simulate a true baseline, I would simulate the exact flow control blade with the inset cavity. No one would design a blade shape with a backward facing step on the suction surface. Therefore, I would have to simulate a blade shape without the inset cavity which changes my flow controlled blade; 2) This flow control technique inherently modifies the blade shape by needing an inset cavity, unlike other techniques that seek to influence the flow by applying suction and blowing to an already existing profile. The technique would inextricably alter any blade shape it was applied to. With reasons 1) and 2) stated above, the goal should be to compare the flow control technique to a blade shape that tries to achieve the same end. Since the baseline shape was used to create the flow controlled shape, particularly

keeping the curvature reasonably the same, the comparison is reasonable.

The baseline case was simulated and the Mach contours are shown in Figure 5. As can be expected, the flow is badly separated on the suction surface starting at approximately 50% chord. The flow controlled blade is shown in Figure 6 for a momentum coefficient of 0.197. The flow remains attached for the entire blade region and appears completely diffused at the exit plane.

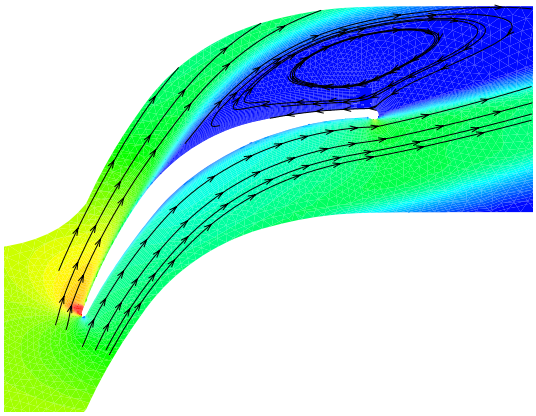

Figure 5 Baseline Blade Mach Contours

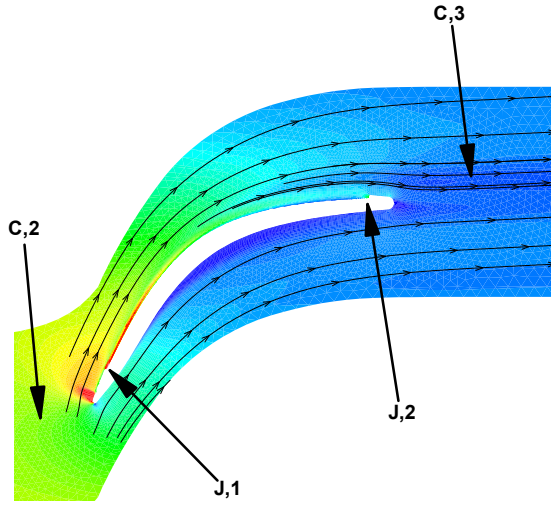

Figure 6 Flow Control Blade Mach Contours

Table 1 summarizes the baseline and flow controlled blade for various momentum coefficients (which were varied by changing the secondary flow injection to core flow total pressure ratios, π_{jc}) and fractional injection slot heights (h/S). Referencing the locations highlighted in Figure 6, the definition of DF used in the table is:

$$DF = 1 - \frac{V_{c,3}}{V_{c,2}} + \frac{\Delta V_y}{2\sigma V_{c,2}} \qquad (2)$$

where ΔV_y is the change in tangential velocity between locations (c,2) and (c,3). Mass averaged quantities were used for the calculation.

The zero momentum coefficient case is for the baseline solution. As the table shows, the circulation and hence the blade loading is increased with increasing values of injection c_μ. The flow controlled blade was able to achieve an axial exit condition for an injection c_μ between 0.179 and 0.197 for the h/s=0.011974 and between 0.134 and 0.146 for h/s=0.00661. The circulation and DF values in Table 1 are plotted in Figure 7. DF will be discussed as a figure of merit throughout the body of text since as mentioned in the introduction, the desire to increase axial compression stage loading places an increased demand on the diffusion requirements of the stator.

Table 1 Flow Control Parameters

c_μ	Γ^*	$\overline{\alpha^M}$	DF	fx100	π_{jc}	h/Sx100
0.	2.09	17.48	0.788	0	1	0
0.179	2.43	2.19	0.967	4.54	1.382	1.1974
0.197	2.50	-1.74	0.976	4.87	1.480	1.1974
0.121	2.35	8.18	0.958	2.85	1.628	0.661
0.134	2.42	2.78	0.972	3.06	1.776	0.661
0.146	2.48	-1.28	0.98	3.25	1.924	0.661

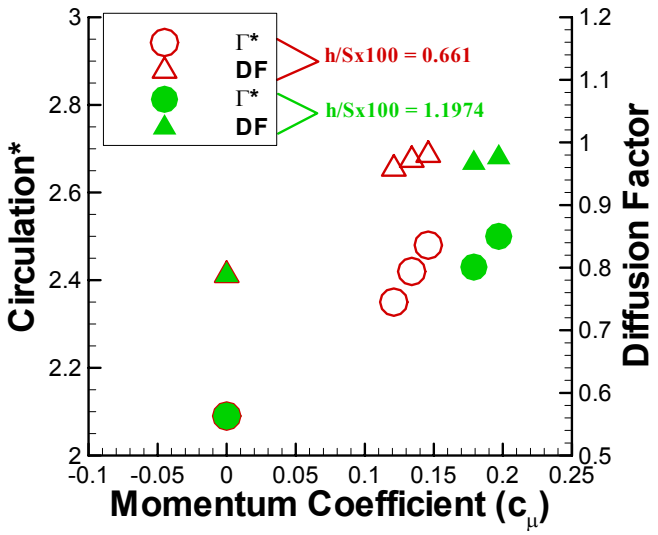

Figure 7 Circulation and DF versus Momentum Coefficient

The slope of the circulation line as a function of c_μ is positive, i.e. $\frac{\partial \Gamma^*}{\partial c_\mu} > 0$. Therefore, as expected the influence on the loading is beneficial and the overall diffusion is greatly increased. The relationship is also seen to be quite linear in the range simulated, although more points would be necessary of course to establish a trend.

The DF and circulation in Figure 7 do not collapse on the injection momentum coefficient for the two different injection slot heights simulated. As can be seen, an offset exists between

the two cases. This can be understood by realizing that the flow control process does not rely solely on injection, but also on the applied suction and that the momentum coefficients for these two areas are quite different. The preceding control volume analysis assumed that the inlet and exit heights (i.e. areas) were the same for the blowing and suction ports in the inset cavity. In reality this is not the case. The suction area needed to be larger than the inlet area to prevent choking and accommodate the required mass flow injected and mixed with the core flow. Therefore, the above plot is particular to the geometry at hand since the x-axis is c_μ for the injection only and does not take into account the separate c_μ for the suction. Another interesting result is that the c_μ=0.146 with h/s=0.00661 achieves a similar DF as the 0.197 with h/s=0.01974 case. Similar results were discovered in the past for flow control airfoils [13,14] which achieved similar lift coefficients for varying injection slot heights and therefore various momentum coefficients. It was a matter of whether you are pressure limited or flow limited in the secondary flow system. A low pressure with a higher flow rate could achieve the same end as a high pressure, low flow rate system. Of course there is most likely a limit in the range over which this applies and certainly there are secondary effects that would make one option more appealing over another, but this appears to be case for the narrow range of geometries and momentum coefficients simulated here.

A parameter that helps to collapse the curves is the isentropic power input of the secondary flow stream. To tie in this analysis with a subsequent stage analysis, Figure 2 and Figure 6 will be used for the subscript nomenclature. The projection of the locations specified in Figure 2 to the CFD simulation is shown in Figure 6. The core inlet and exit conditions are locations (c,2) and (c,3) respectively. Likewise, (j,1) and (j,2) represent the injection and suction of the secondary flow respectively. The fluidic power associated with the total pressure drop between the suction and injection ports can be defined as:

$$P_{j,isen} = \dot{m}_j c_p T_{t,j,2}\left(\pi_j^{\frac{\gamma-1}{\gamma}} - 1\right) \tag{3}$$

The total pressure ratio, π_j, in Eq. (3) is the ratio of the injection to suction slot total pressure. Non-dimensionalizing this equation using the inlet enthalpy flux, $\dot{m}_c c_p T_{t,c,2}$, yields:

$$P^*_{j,isen} = f\tau_{jc}\left(\pi_j^{\frac{\gamma-1}{\gamma}} - 1\right) \tag{4}$$

where τ_{jc} is the temperature ratio between secondary flow suction slot and the inlet core conditions and f is the flow fraction, i.e. ratio of secondary to core mass flow.

Plotting the DF against Eq. (4) using mass averaged values is shown in Figure 8. As is seen, the DF collapses rather well for the two simulations with varying injection slot height. It should be noted that the suction slot height was 1.61 times larger than the injection slot for the h/s=0.00661 case and 2.16 times larger for the h/s=0.011974 case. Interestingly, this suggests that the diffusion enhancement using this technique correlates with the irreversibility (power loss) of the secondary flow stream. Recently, secondary flow stream irreversibility has been presented as a mechanism for the flow vectoring using a counter-flowing secondary flow stream for nozzle flow control [15]. The idea is presented that losses within the secondary stream due to the interaction with the core flow increase the loading, thereby vectoring the flow.

Looking back at Table 1 again also shows that a flow fraction of 4.87% is required for a c_μ of 0.197. A rule of thumb that has emerged over the years has been that a flow control device that uses 0.5 % of the core flow is excessive. This stems from the understanding that 0.5% of the flow would need to be removed or added elsewhere in the cycle and this would be detrimental on the overall engine performance. But, unlike other techniques, the flow is re-circulated rather than added or removed. In order to obtain a better understanding of whether this amount of flow fraction would cause a large penalty on the compression system, both an availability analysis and a simplified power analysis were performed.

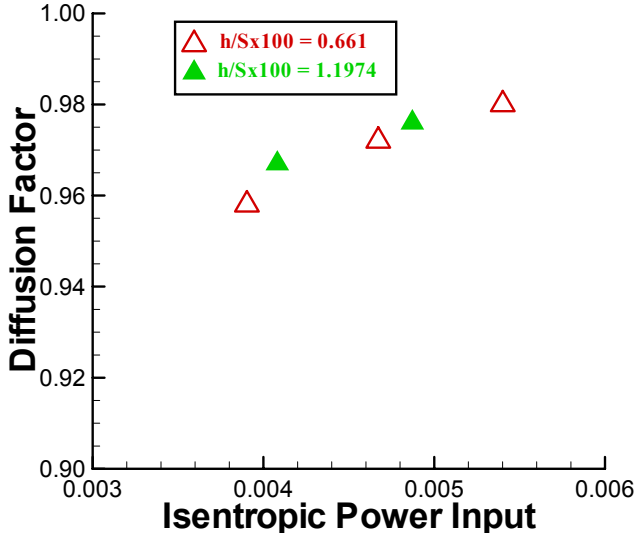

Figure 8 Isentropic Power Input versus DF

AVAILABILITY

A treatise on availability analysis is given in [16]. The availability of a system is defined as:

$$\dot{\Psi} = \dot{m}\left(\Delta H_t - T_t \Delta s\right) \tag{5}$$

where ΔH_t is the change in stagnation enthalpy, T_t is initial starting total temperature and Δs is the change in entropy. The availability is simply the available power extractable at the exit to a system if the system were brought isentropically back to rest at its initial conditions. For a cascade configuration, generally $\dot{\Psi} < 0$ since the cascade is a only a loss producing mechanism with no power input, i.e. $\Delta H_t = 0$ and $\Delta s > 0$. The total availability of a system is the sum of the availability at each boundary to the system.

As before, this analysis will refer to Figure 2 and Figure 6 for the subscript notation. The availability for the CFD simulation at each location is as follows:

$$\begin{aligned}\dot{\Psi}_{c,2} &= 0 \\ \dot{\Psi}_{c,3} &= \dot{m}_c\left(\left(H_{t,c,3} - H_{t,c,2}\right) - T_{t,c,1}\left(s_{c,3} - s_{c,2}\right)\right) \\ \dot{\Psi}_{j,1} &= 0 \\ \dot{\Psi}_{j,2} &= \dot{m}_j\left(\left(H_{t,j,2} - H_{t,j,1}\right) - T_{t,j,1}\left(s_{j,2} - s_{j,1}\right)\right)\end{aligned} \quad (6)$$

Both $\dot{\Psi}_{c,2}$ and $\dot{\Psi}_{j,1}$ are zero since the reference values for these two streams are the conditions at (c,2) and (j,1) respectively. Summing the above relationships to obtain the total availability, simplifying and non-dimensionalizing by the core inlet enthalpy flux yields:

$$\dot{\Psi}^* = \frac{\dot{\Psi}}{\dot{m}_c c_{p,c} T_{t,c,2}}$$

$$\dot{\Psi}^* = \left[\left(\tau_c - 1 - \frac{\Delta s_c}{c_{p,c}}\right) + f\frac{c_{p,j}}{c_{p,c}}\frac{T_{t,j,1}}{T_{t,c,2}}\left(\tau_j - 1 - \frac{\Delta s_j}{c_{p,j}}\right)\right] \quad (7)$$

where c_p is the specific heat at constant pressure and

$$\tau_c = \frac{T_{t,c,3}}{T_{t,c,2}} \qquad \tau_j = \frac{T_{t,j,2}}{T_{t,j,1}}.$$

For the CFD simulation, the secondary flow injection total temperature was equal to the core flow total temperature, i.e. $T_{t,j,1} = T_{t,c,2}$. Also, for simplification, let $c_{p,c} = c_{p,j}$ and the Eq. (7) reduces to:

$$\dot{\Psi}^* = \left(\tau_c - 1\right) + f\left(\tau_j - 1\right) - \frac{\left(\Delta s_c + f\Delta s_j\right)}{c_{p,c}} \quad (8)$$

The first two terms in Eq. (8) represent the work input/loss of the core and secondary stream respectively and the last term the combined irreversibility. The work occurs through the shear work between the core and the secondary flow and although small, is still on the order of the irreversibility term [17]. Therefore, it must be included in the analysis.

The ratio of availability to the baseline availability (i.e. the case with no flow control) is shown in Figure 9 for two different injection slot heights. Mass averaged values were used for the calculations and the exit conditions were integrated at the constant axial location labeled (c,3) in Figure 6. Note that a mass averaged value of the baseline case in this region would be a conservative estimate of the loss since the weighting would be higher for the higher momentum, i.e. non-separated, regions of the flow. In other words, losses would be larger is this flow condition were allowed to mix out.

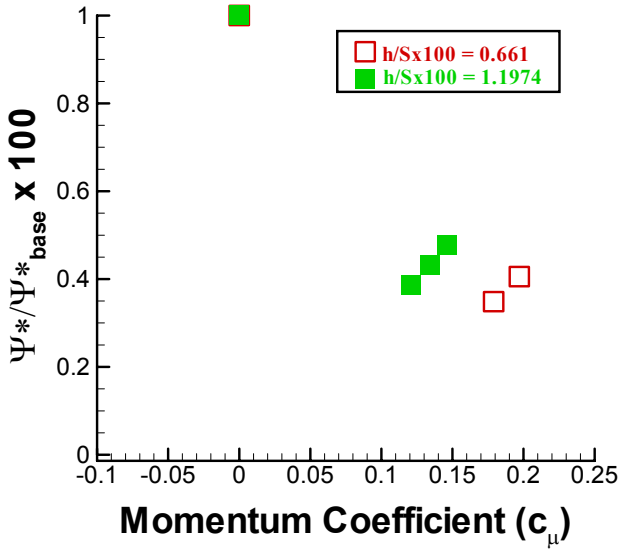

Figure 9 Availability versus Momentum Coefficient

As you can see from Figure 9, for the highest momentum coefficient the availability of the flow control case is approximately 50% less than that of the uncontrolled case. This simply means there is a 50% reduction in the overall loss production with the entrainment and mixing process involved for this flow control technique as compared to the separated baseline case. Thermodynamically this flow control process is more efficient than the separated baseline case, but losses within a delivery system could make the two thermodynamically equivalent. The next section will evaluate the performance of a compression stage that may incorporate this flow control scheme and assess the sensitivity of the stage performance to the secondary flow delivery system efficiency. Keep in mind though, even it were determined that the flow control scheme was found to be thermodynamically equivalent with the separated baseline case due to the inclusion of losses within the delivery system, the flow controlled case still has the advantage of achieving the desired diffusion levels and exit conditions over the uncontrolled baseline.

Another consideration from Figure 9 is that the power loss for the lower c_μ is less than the higher c_μ values. Since $\frac{\dot{\Psi}^*}{\dot{\Psi}^*_{base}} = 1$ when $c_\mu = 0$ then there must exist a value of c_μ where the power loss is a minimum, but does not coincide with the value of c_μ that produces the most diffusion and turning. This may be an artifact of the averaging procedure, but area averaging produced the same trend.

POWER ANALYSIS

An assessment of this technique used in the stage of an axial compression system was performed by analyzing the power input of a stage using this flow control technique in the stator section as shown in Figure 2 and comparing that with the isentropic power input for the same pressure ratio. To obtain the stage design characteristics, a meanline analysis was performed with the goal of a 68 degree rotor exit condition,

1.67 stator solidity and 0.98 stator DF in order to be consistent with the previous results of the CFD analysis. The following meanline input parameters were used:

Table 2 Meanline Input Parameters

$\frac{\dot{m}}{A}$	195.3 kg/s/m^2
Rotor Tip Speed	426.72 m/s
Rotor Work Input	1.62820e5 J/kg
AR_{rotor}	1.1
η_{rotor}	0.90
AVR_{rotor}	0.85
σ_{rotor}	3.0
σ_{stator}	1.67
AVR_{stator}	0.8

The resulting pressure ratio and reaction for the stage was approximately 4.12 and 60/40 respectively. The high rotor solidity was necessary to limit the DF requirement of the rotor and even with this high a solidity, the rotor DF was approximately 0.7.

As shown earlier, Figure 8 gives the non-dimensional power loss of the secondary stream for the flow control process. An adiabatic efficiency may be assigned to this value to account for losses within a "hypothetical" secondary flow delivery system as shown in Figure 2 and give an "actual" power input for the entire secondary flow system, yielding:

$$P^*_{j,actual} = \frac{P^*_{j,isen}}{\eta_j} \tag{9}$$

Combining this with the power input of the rotor and using the definition of adiabatic efficiency gives the total power requirement of the stage shown in Figure 2 as:

$$P = \dot{m}_c c_p T_{t,c,1} \frac{\left(\pi_c^{\frac{\gamma-1}{\gamma}} - 1\right)}{\eta_c} + \dot{m}_c c_p T_{t,c,2} \frac{P^*_{j,isen}}{\eta_j} \tag{10}$$

The first term in Eq. (10) is the power input of the core flow from inlet (c,1) to exit (c,3). The core pressure ratio, π_c, includes the "apparent" loss through the flow controlled stator. Since this flow control technique imparts momentum to the core flow, the "apparent" total pressure loss through the stator is negligible. The CFD simulations of the stator section showed a reduction of only 0.27% in the core mass averaged total pressure for the momentum coefficient of 0.1456. Therefore, the core total pressure ratio, π_c, could be considered equivalent to the rotor pressure ratio.

The core efficiency, η_c, is another matter. This efficiency could be affected by heat transfer from the secondary flow stream to the core flow making the process non-adiabatic through the stator. This violates the assumption made in deriving the overall power input equation which used the definition of adiabatic efficiency for the core flow power input. Also, the less efficient the secondary flow system, i.e. the smaller η_j, the larger the secondary flow injection temperature for a given secondary flow total pressure ratio. This would make the core flow efficiency in this analysis a function of the secondary flow efficiency due to heat transfer effects. An assessment of this effect at this time is not accounted for in this analysis since the CFD simulations presented earlier were performed with the injection total temperature equal to the core flow total temperature. For this analysis, this efficiency will be held at the rotor efficiency value of the meanline analysis, i.e. $\eta_c = \eta_{rotor}$.

Continuing with the analysis, the adiabatic, isentropic power input of the stage is the first term of Eq. (10) with the adiabatic efficiency set to one:

$$P_{isen} = \dot{m}_c c_p T_{t,c,1}\left(\pi_c^{\frac{\gamma-1}{\gamma}} - 1\right) \tag{11}$$

The ratio of Eq. (11), the isentropic power, to Eq. (10), the actual power input, defines an efficiency and is, upon substituting and re-arranging:

$$\eta = \frac{P_{isen}}{P} = \frac{\eta_c}{\left(1 + P^*_{j,isen}\left(\frac{1}{\pi_c^{\frac{\gamma-1}{\gamma}} - 1} + \frac{1}{\eta_c}\right)\left(\frac{\eta_c}{\eta_j}\right)\right)} \tag{12}$$

Figure 10 shows Eq. (12) plotted against the secondary flow system efficiency, η_j. The value for $P^*_{j,isen}$ was chosen from Figure 8 for a DF of 0.98. Two values of overall efficiency are highlighted in Figure 10. There is no particular significance for these two values, they were chosen for comparison purposes only to assess the sensitivity of the overall efficiency to the secondary flow efficiency raised in private discussions [17]. As can be seen, the overall efficiency is 0.883 for a secondary flow system efficiency of 0.7. There is 1.7 points in overall efficiency taken up in powering the secondary flow system. A 28.5% reduction in the secondary flow efficiency, i.e. $\eta_j = 0.50$, results in an overall efficiency of 0.8764, a reduction of 0.75% over the $\eta_j = 0.70$ case. The sensitivity of the overall efficiency to the secondary flow system efficiency is not very large in the $0.5 \le \eta_j \le 0.70$ range for the secondary flow power input under consideration and for this stage configuration. From this simple analysis, the penalty to the stage using this flow control technique does not appear to have a severe impact on performance, even with low secondary flow system efficiency. Although, as mentioned earlier, this does not take into account the non-adiabatic effects due to heat transfer between the secondary flow and core flow.

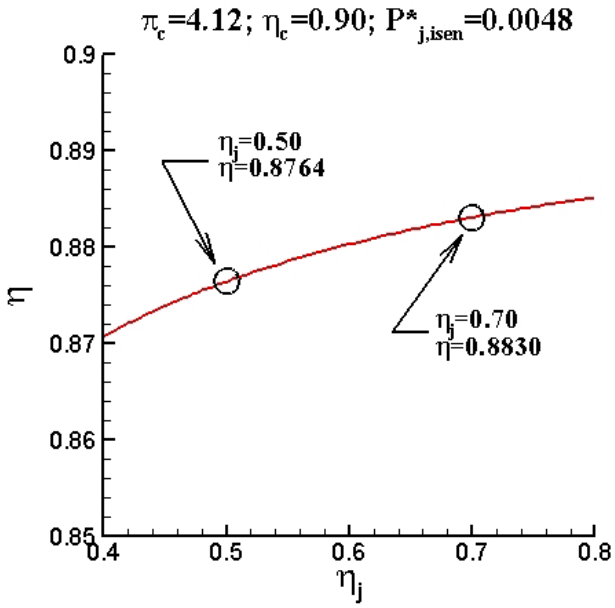

Figure 10 Overall Efficiency vs Secondary Flow System Efficiency

SYSTEM LEVEL ANALYSIS

The overall engine performance implication of utilizing the flow control technique for front fan applications was investigated as part of this effort. A two-spool, mixed-flow, augmented turbofan with a year-2000 production-capable level of technology is used for analysis purposes. Table 3 provides the basic thermodynamic cycle characteristics of this engine, and Figure 11 provides a graphical representation of the geometry/flowpath. (It is important to note that this configuration is notional, and does not represent a fielded engine or an engine in development.)

Table 3 Notional Engine Cycle Characteristics

OPR	20
BPR	0.27
$\dot{m}$	124.7 kg/sec
Throttle Ratio	1.15
Inlet Recovery	0.97
π_{fan}	4.44
η_{fan}	0.87
η_{hpc}	4.51
η_{hpc}	0.86
Maximum T_3	866.5 K
Maximum T_{41}	1894.3K
π_{hpt}	2.29
η_{hpt}	0.88
$f_{hpt,vane,cooling}$	10.00% of core flow
$f_{hpt,blade,cooling}$	5.50% of core flow
π_{lpt}	2.03
η_{lpt}	0.89
$f_{lpt,vane,cooling}$	1.60% of core flow
$f_{lpt,blade,cooling}$	1.40% of core flow
Nozzle CFG	0.95
$Fn_{SLS\text{-}mil}$	98875 N
$Fn_{SLS\text{-}max}$	147841 N
$SFC_{SLS\text{-}mil}$	0.899 kg/hr/daN

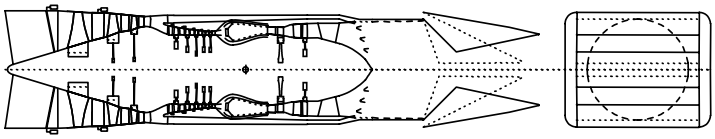

Figure 11 Notional Engine Cross Section

Table 4 describes the pertinent aerodynamic data related to the 3-stage front fan design in the notional engine. Of particular relevance to the current study is the average amount of stator turning at the hub locations.

Table 4 Fan Aerodynamic Parameters of Notional Engine

Corrected Flow / Annulus Area	170.9 kg/sec/m^2
Number of Stages	3
Stage Loading (2gJ(delH)/U^2)	0.83
Inlet Corrected Tip Speed	453.8 m/s
Inlet Physical Tip Speed	454.8 m/s
Exit Hub Speed	324.9 m/s
Average Hub Stator Turning	56.6 deg

In general, without the use of active flow control, separation losses limit the amount of stator turning at the hub location of any stage to ~65 degrees. Through the use of active flow control, this constraint becomes less severe and fan aerodynamic designs with reduced stage count become feasible. The weight savings associated with a stage reduction are countered by thermodynamic losses associated with powering the flow control system. The magnitudes of these savings/losses are quantified as follows.

The compressor map of the fan itself, i.e. all stages, is assumed to be unchanged, and horsepower is extracted from the low-pressure turbine to power the flow control system. Figure 12 shows the effect of low-spool horsepower extraction on thrust and specific fuel consumption (each at sea-level static conditions without the use of an afterburner).

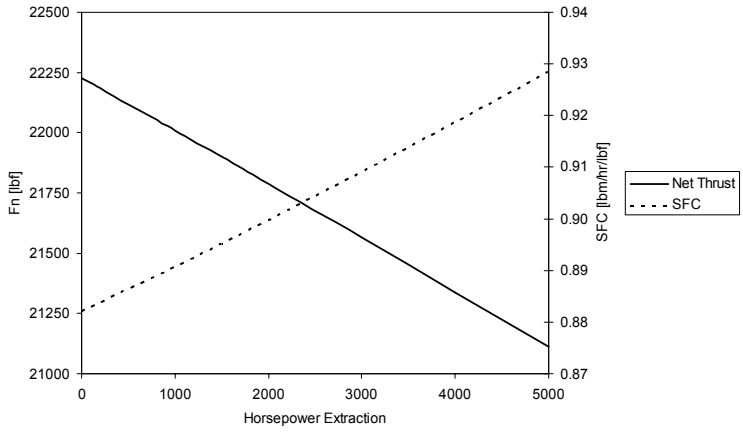

Figure 12 Thrust and SFC versus Secondary Flow Power Extraction

A reasonable assumption for the power required to drive the flow control system is 5% of the fan power in the notional engine. This 5% requirement was arrived at by examining the ratio of the secondary flow power input (second term of Eq. (10)) to core fan power requirement (first term of Eq. (10)) from the 1D power analysis outlined in the previous section:

$$\frac{P_j}{P_c} = P^*_{j,isen}\left(\frac{1}{\frac{\gamma-1}{\pi_c^{\gamma}}-1}+\frac{1}{\eta_c}\right)\left(\frac{\eta_c}{\eta_j}\right) \qquad (13)$$

Using the fan efficiency and pressure ratio from Table 3 along with setting the secondary flow efficiency to 0.5 and $P^*_{j,isen}$ to 0.0048 yields the approximate value of 0.025 for $\frac{P_j}{P_c}$. Multiplying this by two for additional losses (e.g. bearing, shaft, etc.) gives a conservative estimate of 0.05 or 5%.

Will all this in mind, this yields a requirement of approximately 1120 kW, and results in a (dry) net thrust loss of 1463 N and specific fuel consumption (SFC) increase of 0.013 kg/hr/daN. (Note that at sea level static in full afterburner with 1120 kW extraction, the net thrust loss is 1730 N when compared to the notional engine in full afterburner.)

A reduction in the number of fan stages from 3 to 2 will result in a fan weight savings in the 1112-1245 N regime. Figure 13 shows the influence of average stage loading coefficient on 1st stage stator turning angle at the hub location. For loadings above 0.95, Figure 13 shows that a two stage design will require an amount of hub stator turning greater than 65 degrees. The relative Mach number at the first stage rotor tip is shown for the 2 and 3 stage designs as a function of loading coefficient in Figure 14. The average stage loading coefficient must increase from 0.8 to 1.4 in order for the 2 stage design to have the same 1st stage rotor tip relative Mach number as the 3 stage design. An increase in average stage loading coefficient implies a higher stator diffusion requirement, an environment in which flow control can help.

The system level analysis suggests that active fan flow control can be used to increase overall engine thrust to weight. The notional engine had a thrust-to-weight ratio of 5.62. A replacement of the 3 stage front fan with a 2 stage design that incorporates active flow control will, despite the thermodynamic losses, yield an overall engine thrust-to-weight improvement to the 5.80 regime. Further analysis is required to quantify the benefit for other engine cycles, particularly ones that involve fixing the engine volumetric size and allowing for higher OPR. It is in these cycles that one may see a SFC benefit while maintaining or slightly increasing the thrust to weight ratio.

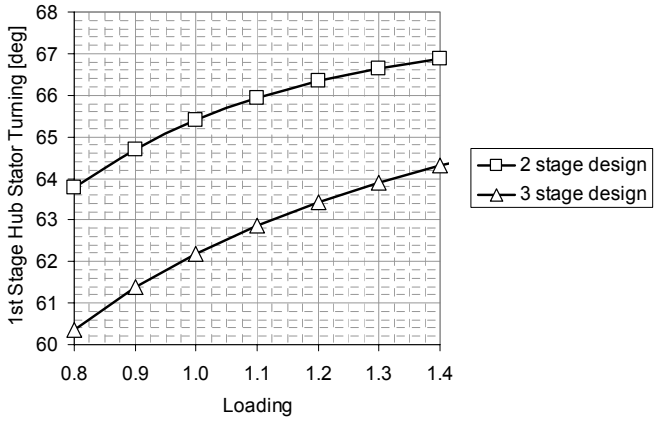

Figure 13 First Stage Stator Hub Turning versus Loading

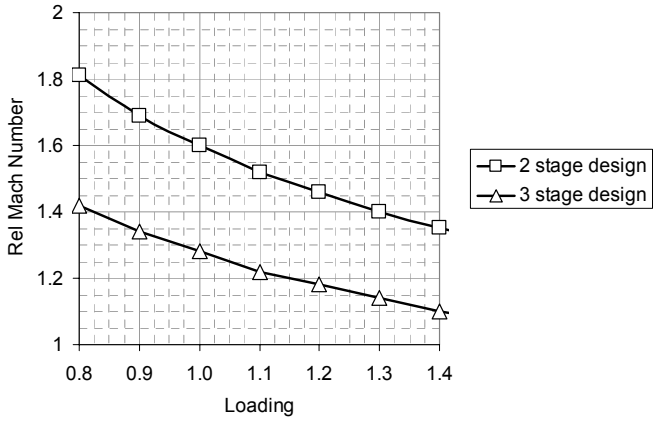

Figure 14 Relative Mach Number versus Loading

EXPERIMENTAL RESULTS

Cascade

A cascade was created by simply extruding the cross section outlined earlier with internal cavities sufficiently sized to provide the necessary mass flow to feed the injection and suction slots on the blade surface. The blade section with the larger injection slot height to pitch ratio (h/s) of .011974 was chosen. The cross section of the cascade is shown in Figure 15 and the solid model in Figure 16. Secondary flow to the cascade is provided from only one side of the blade to allow viewing from the other side of the cascade test section for DPIV measurements. Also, this would be the intended configuration for a stage as shown in Figure 2. Although, the blade cross section provided sufficient area to accommodate the necessary mass flow, it was equal to the respective slot areas to

which they supplied air flow. Ideally one would want the cross sectional areas supplying the secondary flow to be larger, but that was not possible due to geometric constraints and structural rigidity considerations. Although manufacturing the cascade using EDM technology is a fairly easy task, a minimum wall thickness is required to prevent warping and maintain tolerances.

The blowing and suction supply cavities need to be located within the central portion of the blade cross section since this portion of the blade provides sufficient metal thickness. With the blowing and suction slots located to the ends of the blade, this requires the internal flow to negotiate an undesirable 180 degree turn as can be seen in Figure 15. Unfortunately, without very careful design considerations in this region, this will result in significantly more loss generation. Insufficient time did not allow for any detailed analysis of this area. With all the geometric, manufacturing and time constraints, the cross section in Figure 15 is considered the best that could be done.

The cascade test section is six inches tall and contains six blades across the test section with a blade pitch of 0.0762 meters. The blade chord measured as a straight line from leading to trailing edge is 0.127 meters giving a solidity of 1.67. The cascade inlet Mach number was 0.7 with an inlet angle of 68 degrees.

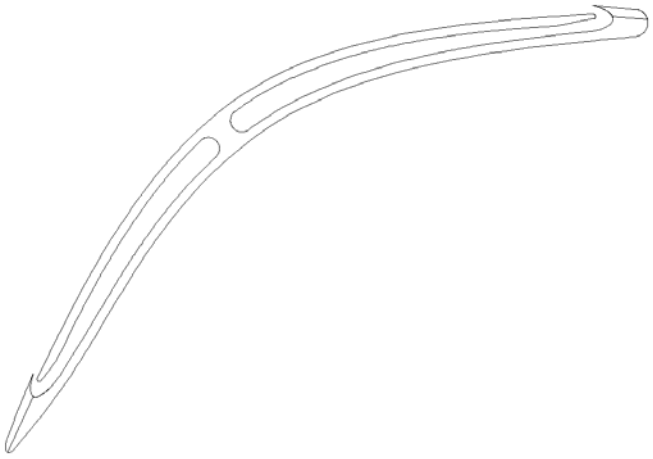

Figure 15 Flow Control Cascade Cross Section

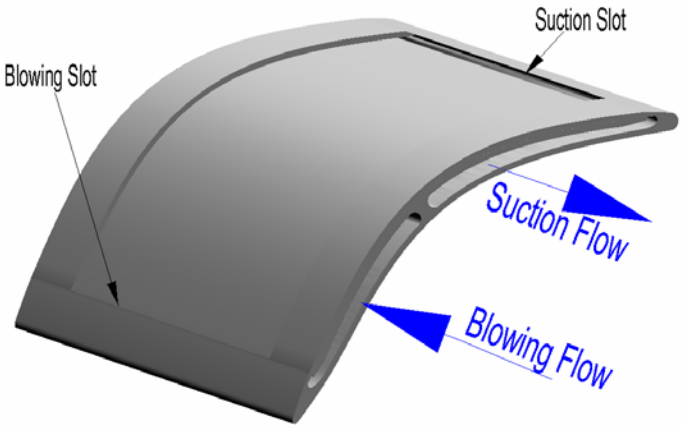

Figure 16 Flow Control Cascade

Secondary Flow System

General Layout

The secondary flow system is created using a centrifugal automotive supercharger powered by an electric motor and controlled by an AC inverter. Figure 17 gives a schematic of this system along with measurements made at various stations along the flowpath of the system. The by-pass valve shown will be explained later.

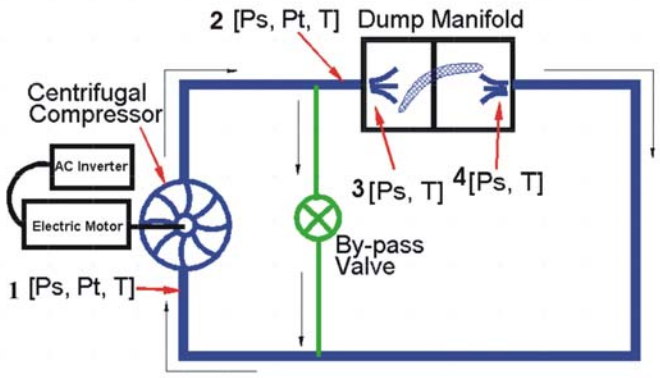

Figure 17 Experimental Secondary Flow Circuit

The supercharger was chosen because it could provide the desired pressure ratio and power input for the momentum coefficients of interest. It was difficult to locate a supercharger with sufficient surge margin for the flow rate of interest. The cascade corrected flow rate is approximately 4.80 kg/sec. Since only 4 blades out of the 6 (i.e. 5 passages) are controlled, the flow rate that needs to be controlled is 3.84 kg/sec. The desired fraction of secondary flow to core flow (i.e. flow fraction, f) from Table 1 is 0.0454, which means that the required corrected flow rate for the secondary flow system is 0.174 kg/sec. Searching all the available centrifugal supercharger maps puts this flow rate very close to the surge line for the even the smallest supercharger that could provide the necessary pressure ratio. A detailed map of the supercharger chosen for this experiment was not available, but a map of a "very close" competitor with "similar performance" was obtained and verified that it would be operating very close to surge at this flow rate.

The desired pressure ratio of the secondary flow system from Table 1 is approximately 1.48. This pressure ratio is the ratio of the blowing jet flow total pressure to the core flow total pressure. In actuality, the secondary flow system pressure ratio is equal to the ratio of the suction slot total pressure to the inlet blowing slot total pressure. This pressure ratio is approximately 1.4. But this pressure ratio does not take into account any flow losses within the secondary flow system.

Due to short period of time afforded for the design of the secondary flow system, a simple dump manifold was created to supply the air to the cascade section. Figure 18 shows a picture of the dump manifold with the cover removed. Of course this type of manifold is not desirable from a loss perspective, so an analysis was conducted to determine the required pressure ratio of the centrifugal compressor needed to deliver a 1.4 pressure ratio on the cascade blade. The loss analysis showed that the centrifugal compressor needed to supply a pressure ratio on the order 1.9 to achieve the desired blowing total pressure. This places the compressor in surge for a corrected flow rate of

0.174 kg/sec. Therefore, a by-pass valve was added to the system as shown in Figure 17 to re-circulate flow and keep the centrifugal compressor from surging while providing sufficient pressure ratio to the secondary flow. This assumes that the inlet blowing slots for the flow control are choked and that re-heating effects of the re-circulating secondary flow for the short blow down test time of approximately 10 seconds would not have a significant effect.

Drive System

The approximate amount of power required for the secondary flow system can be calculated from a simple 1D analysis as carried out in the previous sections and re-written here:

$$P = \dot{m} c_p T_t \frac{\left(\pi^{\frac{\gamma-1}{\gamma}} - 1 \right)}{\eta} \qquad (14)$$

The blow-down tunnel is a pressurized system. The total pressure is anywhere from 1.378-1.723x10^5 Pa from past experience with the specified inlet condition to this cascade. The tunnel total temperature can be approximated as a standard day condition. With this tunnel total pressure and temperature and a corrected mass flow of 0.174 kg/sec, the actual mass flow in the secondary system may vary between 0.238 kg/sec to 0.295 kg/sec. Approximating the compression efficiency to be 70% from a comparable compressor map would lead to a power requirement of 18.64 to 23.86 kW. A 3400 RPM, 37.28 kW, 460 Volt, 3 phase electric motor was chosen to be sufficient for the experiment controlled by an AC inverter capable of continuous 44.74 kW control. .

The power transmission to the supercharger was accomplished by using a high precision timing pulley and belt arrangement. The supercharger speed needed to be approximately 42,000 rpm in order to achieve the required pressure ratio. There is an internal step up within the supercharger of 4.1:1 thereby requiring an external pulley arrangement of 3:1 using a maximum motor speed of 3400 RPM. At these speeds, stock steel pulleys are close to their maximum rim speed, but a system was found that could transmit the required power and was used successfully in the experiment.

DPIV Results

The desired inlet conditions for the cascade test were an inlet angle of 68 degrees and Mach number of 0.7. Unfortunately, the secondary flow system choked at less than half the desired flow rate of approximately 0.238 kg/sec. A simple test was performed to determine which part of the secondary flow system was limiting the flow rate. Two of the blade surface injection slots were taped off and the flow rate remained unchanged. The tape was removed and two of the blade surface suction slots were taped off which in turn halved the flow rate. Therefore, from this simple analysis it was determined that the somewhere within the suction side of the secondary flow system choking occurred. Currently a CFD analysis of the blade passages is being performed to determine where within the suction portion of the secondary flow system this occurred.

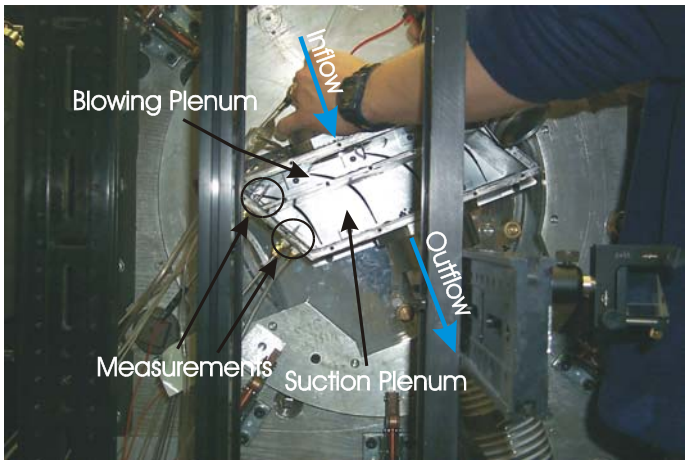

Figure 18 Dump Manifold Picture

With the limited amount of flow rate in the secondary system, the inlet Mach number to the cascade was lowered to 0.3 in order to try and match the flow fraction and momentum coefficient of 0.454 and 0.197 respectively of the CFD simulations outlined earlier. This was the lowest Mach number the cascade tunnel could run stably. Also, to achieve the desired pressure ratio of 1.87 within the secondary flow system, the by-pass valve was slightly opened to re-circulate a fraction of the flow prior to the manifold to keep the supercharger from surging. An attempt was made to calculate a momentum coefficient by measuring the static pressure at the endwalls on each side of the blade injection slots. One could then calculate a momentum coefficient assuming the total pressure and temperature measurement within the blowing plenum portion of the dump manifold shown in Figure 17 (location 3 in the figure) to be the total pressure and temperature at the injection slot. Unfortunately, the thermocouple measurements used to determine the total temperature at the inlet to and within the blowing plenum of the dump manifold failed during the test.

Data taken for the secondary flow system prior to the test showed that the supercharger could operate in the by-pass configuration at an approximate adiabatic efficiency of 0.65 for a total pressure ratio of 1.8. This was the operating condition chosen for the test. The measured inlet temperature to the supercharger at this operating condition during the test was 309 K. Assuming an adiabatic efficiency of 0.65 with a total pressure ratio of 1.8 puts the exit temperature of the supercharger at 396 K. With this temperature, along with the measured total and static pressure prior to the blowing plenum (location 2 in Figure 17) to calculate the mass flow of the secondary system, yielded a secondary mass flow rate of 0.0716 kg/sec. The uncertainty in this calculation was determined to be ±0.001738 kg/sec. The core flow rate for the blow down tunnel operating at a Mach number 0.3 was calculated to be 2.0 kg/sec. This yields a flow fraction of secondary to primary flow of 0.0358. This is approximately 1% of the core flow less than the desired value of 0.0454. It was also noted that measurements taken prior to the failure of the thermocouples showed a significant heat loss in the dump manifold. That combined with the failure of the temperature measurements during the test made any attempt to calculate the momentum coefficient unreliable.

Figure 19 shows the interrogation regions for the DPIV measurements. The interested reader is pointed to

references [2,18] for a more detailed look at the DPIV setup. Only regions A, B and C were obtained due to time constraints.

There are many factors associated with the DPIV uncertainty-calculation process (laser, CCD, seeding, imaging, algorithms, oscilloscope, etc). The highest uncertainty was found to be associated with the velocity calculation which involves Δx (the displacement in pixels of each interrogation region), Δt (the time interval between the two exposures), and the magnification of the digital image relative to the object (pix/m). The displacement in pixels obtained by peak-locator algorithms can provide sub-pixel accuracy (< 0.1 pixels) after correction for various biases. The Δt was adjusted to yield typical displacements of the main stream > 10 pixels, and the uncertainty is thus < 1%. Values in the wake region, however, may have higher uncertainties due to the lower Δx. The maximum uncertainty in the Δt was calculated from the time interval between the two laser pulses with the aid of an oscilloscope (uncertainty 2%). It was found that this uncertainty increases with lower laser power and with lower Δt. A conservative number for the present experiments, which employed a Δt of about 4 μs and powers around 10 mJ, was found to be <1%. The magnification was measured using images of grids located in the laser-sheet plane to better than 1%. Combining these conservative measurements of uncertainty yields a maximum error of < 2% for the free-stream regions and ~10% in the low speed areas such as the wake region.

A composite image of the interrogated regions for the baseline case (i.e. no flow control) is shown in Figure 19.

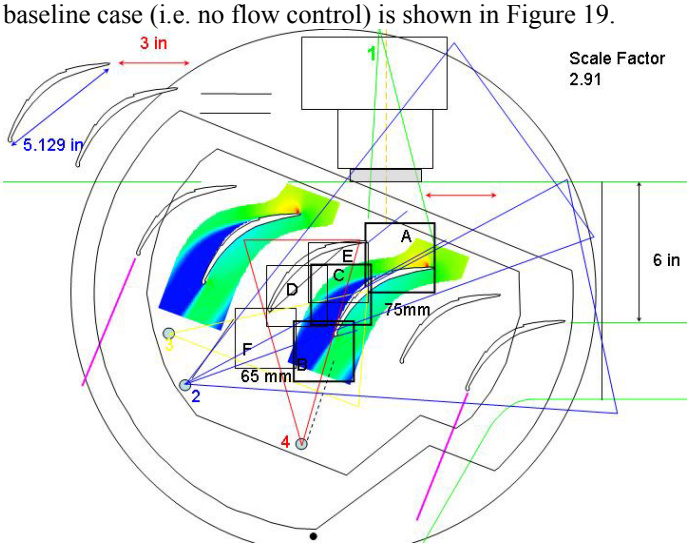

Figure 19 DPIV Interrogation Regions

As you can see, a significant amount of separation occurs along the suction surface of the blade. Similarly, a composite image of the controlled blade is shown in Figure 20. Again, separation is seen, but at a significantly lower level over the baseline case, showing that the control is having a desirable effect.

Significant difference were seen in the injection slot static pressure measurements taken at each endwall which leads to the conclusion of very non-uniform injection and a high probability for non-uniform suction. A detailed 3D CFD analysis is underway to model this cascade section and preliminary results are confirming this hypothesis. Any radial injection would imply a reduction in momentum coefficient aligned with the core flow. A subsequent redesign which will seek to provide injection and suction uniformity will follow the analysis.

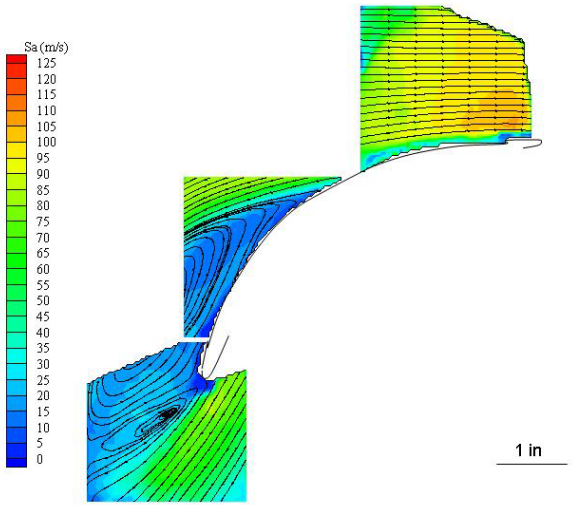

Figure 20 DPIV Experimental Baseline Composite DPIV Image

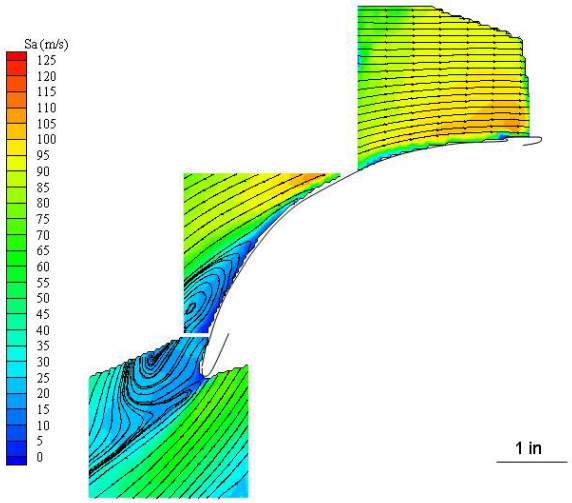

Figure 21 Experimental Flow Control Composite DPIV Image

CONCLUSIONS

A continuous steady flow control concept using an inset cavity and pumping system to continually re-circulate a secondary flow which in turn enhances the core flow diffusion was presented. A control volume analysis was performed to find relevant non-dimensional parameters and a CFD simulation executed varying those parameters showed that an apparent DF of 0.98 could be achieved. The word "apparent" is used because the secondary flow control stream adds momentum to the core flow with the secondary flow system requiring work input through a pumping system. The "penalty" for the secondary system is addressed with a simple power and availability analysis. The availability analysis showed that the process involved with this technique resulted in approximately

a 50% lower power loss through the stator over the separated baseline case. This analysis included the losses within the secondary flow stream, but did not account for losses within a delivery system of this secondary flow. This means that thermodynamically this flow control process is more efficient than the separated baseline case, but losses within a delivery system could make the two thermodynamically equivalent. Even with thermodynamic equivalence, the flow controlled case still has the advantage of achieving the desired diffusion levels and exit conditions over the uncontrolled baseline. The 1D power analysis was used to assess this technique's impact on the efficiency of an axial compression stage and the sensitivity of this efficiency to the secondary flow system's efficiency. A stage with a pressure ratio of 4.12 and a compressor adiabatic efficiency of 0.90, yielded an overall efficiency of 0.883 for a secondary flow system efficiency of 0.7. Lowering the secondary flow system efficiency to 0.5 gave a 0.876 overall efficiency. The sensitivity of the overall efficiency to the secondary flow system efficiency was not excessively large. Therefore, it may be feasible to achieve a 4.0 pressure ratio with a 0.88 adiabatic efficiency.

Also, a system level analysis is presented to assess the merits that may be realized in a notional engine with this type of flow control. The notional engine contained a 3 stage fan which was replaced by a 2 stage fan using flow control. The power to drive the flow control system was taken off the low pressure turbine. For this preliminary study, an engine fuel consumption penalty and a thrust-to-weight benefit were realized with a specific fuel consumption and thrust-to-weight ratio increase of 1.5% and 3.2% respectively.

A cascade experiment was performed to demonstrate the concept and was conducted in a blow-down cascade tunnel. The secondary flow system was designed using an automotive supercharger driven by an electric motor to provide continuous re-circulating flow. The experiment was not successful in providing the simulated levels of diffusion due to flow limitations, i.e. choking, within the suction portion of the flow control scheme. Even with this limitation, significant improvements in diffusion were qualitatively seen from the DPIV measurements. It is believed that non-uniform injection and suction led to the less than expected behavior of the flow control technique. A 3D CFD analysis is ongoing and preliminary findings are showing large injection and suction non-uniformities. A redesigned cascade section with improved injection and suction characteristics will follow.

ACKNOWLEDGMENTS

The authors would like to thank Techsburg in Blacksburg for their dedication during experimental testing and what turned out to be a very long week.

NOMENCLATURE

AR	aspect ratio
AVR	axial velocity ratio
BPR	bypass ratio
c_μ	injection momentum coefficient
C_p	static pressure rise coefficient
DF	diffusion factor
f	flow fraction
h/S	ratio of injection slot height to pitch
F	integrated loading
Fn	thrust
H_t	stagnation enthalpy
$\dot{m}$	mass flow
$\frac{\dot{m}}{A}$	specific mass flow
V	velocity magnitude
OPR	overall pressure ratio
P	power
S	pitch
s	entropy
SFC	specific fuel consumption
$\overline{\alpha^M}$	mass averaged flow angle
Γ	circulation
η	adiabatic efficiency
π	total pressure ratio
σ	solidity
ρ	density
τ	total temperature ratio
$\dot{\Psi}$	availability

Subscripts

c	core flow
j	secondary flow
x	axial direction
y	tangential direction
t	stagnation condition
fan	Fan
hpc	high pressure compressor
hpt	high pressure turbine
lpt	low pressure turbine
sls	sea level static conditions

REFERENCES

1. Bons, J.P., Sondergaard, R., Rivir, R.B., 2000, "Turbine Separation Control using Pulsed Vortex Generator Jets," ASME Paper No. 2000-GT-0262.
2. Estevadeordal, J., Copenhaver, W., Car, D., Koch, P., Ng, W., Guillot, S., Carter, C., 2002, "Macro- and milli-DPIV Studies of a Boundary-layer-based Flow-control System for a Transonic Cascade," 11th Intl. Symp. On Apll. Of Laser Techniques to Fluid Mechanics, Lisbon.
3. Farokhi, S., 1998, "Propulsion system design with smart vortex generators", Aircraft Design, **1**, pp. 127-143
4. McCormick, D. C., 2000, "Boundary Layer Separation Control with Directed Synthetic Jets," AIAA Paper No. 2000-0519.
5. McMichael, J.M., 1996, "Progress and Prospects for Active Flow control Using Microfabricated Electro-Mechanical Systems (MEMS)," AIAA Paper No. 96-0306.

6. Smith, B. and Glezer, A., 2002, “Jet Vectoring Using Synthetic Jet Actuators,” J. Fluid Mech., **458**, pp. 1–34.
7. Roth, J. R., D. M. Sherman, and S. P. Wilkinson, 1998, “Boundary Layer Flow Control with a One Atmosphere Uniform Glow Discharge”, AIAA Paper No. 98-0328.
8. Strykowski, P. J., Krothapalli, A., Forliti, D. J., 1996, "Counterflow thrust vectoring of supersonic jets," AIAA J., **34**, 2306.
9. Strykowski, P. J., Krothpalli, A., 1993, “The Countercurrent Mixing Layer- Strategies for Shear-Layer Control,” AIAA Paper No. 93-3260.
10. Strykowski, P. J., Krothapalli, A., Jendoubi, S., 1996, “The Effect of Counterflow on the Development of Compressible Shear Layers,” J. of Fluid Mech.,” **308**, pp. 63-96.
11. Van der Veer, M. R., Strykowski, P. J., 1997, “Counterflow Thrust Vector Control of Subsonic Jets: Continuous and Bistable Regimes,” J. of Propulsion and Power, Vol. **13**(3), pp. 412-420.
12. Personal communications, GE Aircraft Engines, Cincinnati, OH, 2002.
13. McLachlan, B. G., 1989, “Study of a Circlulation Control Airfoil with Leading/Trailing-Edge Blowing”, J. Aircraft, **26**(9), pp. 817-821.
14. Shrewsbury, G. D., 1989, “Numerical Study of a Research Circulation Control Airfoil Using Navier-Stokes Methods,” J. Aircraft, **26**(1), pp. 29-32.
15. Forliti, D. J., Strykowski, P.J., Gillgrist, R. D., 2002, “The Role of Irrerversibility in Vectoring Thrust Using Counterflow Control”, AIAA Paper No. 2002-2950.
16. Van Wylen, G. J., Sonntag, R. E., 1973, *Fundamental of Classical Thermodynamics, 2nd Ed.,* John Wiley and Sons, New York, NY, pp. 282-288.
17. Personal communications, MIT Gas Turbine Lab, Boston, MA, 2003.
18. Estevadeordal, J., Gogineni, S., Goss, L., Copenhaver, W. and Gorrell, S., 2002, “Study of Wake-Blade Interactions in a Transonic Compressor Using Flow Visualization and DPIV,” ASME J. of Fluids Engineering, **124**, pp. 166-175.